Crystal field excitations from Yb^{3+} ions at defective sites in highly stuffed $Yb_2Ti_2O_7$

G. Sala,[1,2,*] D. D. Maharaj,[2] M. B. Stone,[1] H. A. Dabkowska,[3] and B. D. Gaulin[2,3,4,†]

[1]*Neutron Scattering Division, Oak Ridge National Laboratory, Oak Ridge, Tennessee 37831, USA*

[2]*Department of Physics and Astronomy, McMaster University, Hamilton, Ontario, Canada L8S 4M1*

[3]*Brockhouse Institute for Materials Research, McMaster University, Hamilton, Ontario, Canada L8S 4M1*

[4]*Canadian Institute for Advanced Research, 661 University Avenue, Toronto, Ontario, Canada M5G 1M1*

(Received 18 October 2017; revised manuscript received 23 February 2018; published 11 June 2018)

The pyrochlore magnet $Yb_2Ti_2O_7$ has been proposed as a quantum spin ice candidate, a spin liquid state expected to display emergent quantum electrodynamics with gauge photons among its elementary excitations. However, $Yb_2Ti_2O_7$'s ground state is known to be very sensitive to its precise stoichiometry. Powder samples, produced by solid-state synthesis at relatively low temperatures, tend to be stoichiometric, while single crystals grown from the melt tend to display weak "stuffing" wherein ∼2% of the Yb^{3+}, normally at the A site of the $A_2B_2O_7$ pyrochlore structure, reside as well at the B site. In such samples Yb^{3+} ions should exist in defective environments at low levels and be subjected to crystalline electric fields very different from those at the stoichiometric A sites. Neutron scattering measurements of Yb^{3+} in four compositions of $Yb_{2+x}Ti_{2-x}O_{7-y}$ show the spectroscopic signatures for these defective Yb^{3+} ions and explicitly demonstrate that the spin anisotropy of the Yb^{3+} moment changes from XY-like for stoichiometric Yb^{3+} to Ising-like for "stuffed" B site Yb^{3+} or for A site Yb^{3+} in the presence of oxygen vacancies.

DOI: 10.1103/PhysRevB.97.224409

I. INTRODUCTION

Exotic magnetic ground states of cubic pyrochlore magnets, with the composition $A_2B_2O_7$, are of great topical interest, as the pyrochlore lattice is one of the canonical architectures supporting geometrical frustration in three dimensions [1,2]. Magnetism can reside at either the A^{3+} site or the B^{4+} site, and the magnetic moments' anisotropy and the interactions between the moments conspire to give rise to rich ground-state selection. Among the states and materials that have been of recent interest are the classical spin ice states in Dy and Ho titanate pyrochlores [3–7], spin liquid and spin glass states in molybdate pyrochlores [8], and spin fragmentation in Nd-based zirconate pyrochlores [9]. The possibility that a quantum analog of the spin ice ground state, i.e., quantum spin ice (QSI), may exist in certain low-moment pyrochlore magnets, including $Yb_2Ti_2O_7$ and $Pr_2Zr_2O_7$, has generated much excitement [10–23].

At low temperatures $Yb_2Ti_2O_7$ displays two magnetic heat capacity anomalies: a broad one near 2 K and a sharp anomaly signifying a thermodynamic phase transition near $T_C = 0.26$ K [24–28]. The thermodynamic phase transition near $T_C = 0.26$ K is generally thought to be to a splayed ferromagnet, with moments pointing close to 100 directions [29–32]. However, surprising sample variability has been reported in this phase transition, with some studies not seeing direct evidence for the ferromagnetic ordered state [16,33–39]. Using the sharp anomaly in C_P as the figure of merit for the phase transition, interesting systematics have been observed [27,28,40,41]. Powder samples produced by solid-state synthesis at relatively low temperatures show a sharp C_P anomaly and a high T_C, usually ∼0.26 K [27,28,40]; however, most single-crystal studies display broader thermodynamic anomalies at much lower temperatures, often with T_C around and below 0.2 K [29,30,42,43].

Crystallographic studies of the powder and single-crystal samples have revealed that the powder samples are stoichiometric $Yb_2Ti_2O_7$, while the single crystals are "lightly stuffed" [27]. They are characterized by the composition $Yb_{2+x}Ti_{2-x}O_{7-y}$, with $x \sim 0.05$ [27]. That is, a small excess of Yb^{3+} ions, nominally at the crystallographic 16d or A site, is "stuffed" onto the 16c or B site where nonmagnetic Ti^{4+} ions are located in pure $Yb_2Ti_2O_7$, as schematically indicated in Fig. 1. It is remarkable that such a small change in stoichiometry could so strongly affect the ground-state selection of a simple ordered state in a three-dimensional magnetic insulator. A related phenomenon has also recently been observed in the effect of hydrostatic pressure on stoichiometric $Yb_2Ti_2O_7$ samples, where ambient pressure conditions show no sign of a muon spin rotation (μSR) signal for the transition, but a minimal 1 kbar (and above) applied pressure results in a clear signal for a transition near $T_C \sim 0.26$ K [44].

With weak stuffing able to suppress this phase transition by as much as ∼25% [27–30,40] in this topical material, it is important to understand precisely what is at play in its ground-state selection. One thing that is clear is that most single crystals of $Yb_2Ti_2O_7$ likely have Yb^{3+} ions occupying not only the stoichiometric A sites but also B sites. They also possess A sites with missing oxygen neighbors. These Yb^{3+} ions in defective environments are expected to experience very different crystal field effects than those at stoichiometric A sites [45]. As the spin anisotropy and size of Yb^{3+} moment are determined by

*salag@ornl.gov

†bruce.gaulin@gmail.com

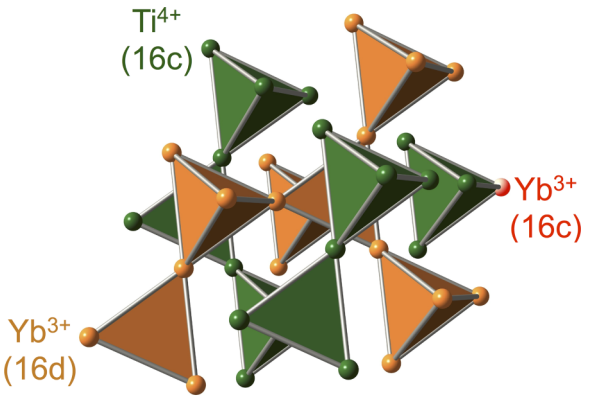

FIG. 1. The pyrochlore lattice, displayed by $A_2B_2O_7$ compounds, belongs to the $Fd\bar{3}m$ space group and consists of two interpenetrating networks of corner-sharing tetrahedra. In stoichiometric $Yb_2Ti_2O_7$, the A sublattice is occupied by rare-earth magnetic Yb^{3+} ions (orange spheres), and the B sublattice is occupied by a nonmagnetic Ti^{4+} site (green spheres). In stuffed $Yb_{2+x}Ti_{2-x}O_{7-y}$, a small fraction of Yb^{3+} ions (in red) also occupy the B sites, and they experience a different crystalline electric field due to the different local environment of surrounding ligands at the B site compared with the A site.

such crystal field effects, it is possible that the defective Yb^{3+} moments and their anisotropy are very different from those of stoichiometric Yb^{3+}; indeed, a prediction from point-charge calculations of the crystal field effects on Yb^{3+} has already suggested that this is the case [45].

The eigenvalues and eigenfunctions associated with crystal field states can be determined using inelastic neutron spectroscopy, and indeed, these have been determined for stoichiometric $Yb_2Ti_2O_7$ and several other rare-earth-based pyrochlore magnets [45–48]. However, the equivalent measurements on Yb^{3+} in defective environments in $Yb_{2+x}Ti_{2-x}O_{7-y}$ are much more difficult, as the environments occur at low density in these materials. Additionally, as we will see, the eigenvalues associated with the defective environments tend to extend to much higher energies. These difficulties necessitated the use of the most modern neutron sources and instrumentation to tackle this problem.

II. EXPERIMENTAL TECHNIQUES

For clarity, we shall refer to the $x = 0$ and $x = 0.05$ samples as the stoichiometric and lightly stuffed samples, respectively. The newly synthesized samples with stuffing levels of $x = 0.12$ and $x = 0.19$ will be referred to as the highly stuffed samples henceforth. It should be noted that all "stuffed samples" are crushed single crystals, and they will be collectively described as such in this work. The sample preparation and characterization of the stoichiometric ($x = 0$) and lightly stuffed ($x = 0.05$) samples of $Yb_{2+x}Ti_{2-x}O_{7-y}$ are described elsewhere [27]. Two rods of $Yb_{2+x}Ti_{2-x}O_{7-y}$ with composition $x = 0.12$ and $x = 0.19$ and dimensions $50 \times 6 \times 6\ mm^3$ were prepared by solid-state reaction between pressed powders of Yb_2O_3 and TiO_2 which were sintered at 450 °C for 15 h with warming and cooling rates of 100 °C/h. The purity of the starting powders of Yb_2O_3 and TiO_2 was close to 99.999%. To produce highly stuffed samples of $Yb_{2+x}Ti_{2-x}O_{7-y}$, a higher ratio of Yb_2O_3 to TiO_2 was used in comparison to what is conventionally used in order to produce stoichiometric samples of $Yb_2Ti_2O_7$. The two single crystals were grown from these rods at McMaster University by utilizing the floating-zone image furnace technique, which is described elsewhere [49]. The growths were conducted in O_2 gas with no overpressure, and the growth rates were 7 and 8 mm/h for the $x = 0.12$ and $x = 0.19$ samples, respectively. Each of the single-crystal samples was then crushed with a mortar and subsequently pulverized using a Pulverisette 2 mortar grinder for 30 min to produce the highly stuffed powder samples. The resulting samples were ≈4 g each. The chemical compositions of these two highly stuffed powders were fully characterized using the neutron powder diffractometer POWGEN [50] located at the Spallation Neutron Source at Oak Ridge National Laboratory (ORNL). The crystallographic refinement was performed using JANA2006 [51] and FULLPROF [52] crystallographic refinement software. Our best refinement of these powder diffraction data gives $x = 0.122(4)$ and 0.192(3), with oxygen vacancies located preferentially on the O(1) sites of the pyrochlore lattice, in agreement with Ref. [53].

Inelastic neutron scattering measurements were performed on these highly stuffed samples. We studied their crystal electric field (CEF) excitations using the direct geometry time-of-flight spectrometer SEQUOIA [54] at ORNL. The highly stuffed powder samples were loaded into aluminum flat plates with dimensions $50 \times 50 \times 1\ mm^3$ and were sealed with indium wires under He atmosphere in a glove box. An empty aluminum flat plate with the same dimensions was prepared in a similar manner and employed for background measurements. The empty plate together with the two highly stuffed powder samples were loaded on a three-sample changer in a closed-cycle refrigerator. Measurements were performed at $T = 5$ and 200 K, with incident energies of $E_i = 150, 250$, and 500 meV. The corresponding chopper settings selected for the T_0 chopper, which blocks fast neutrons, and the fine-resolution chopper, FC_2, selected at these energies were $T_0 = 150$ Hz and $FC_2 = 600$ Hz, $T_0 = 120$ Hz and $FC_2 = 600$ Hz, and $T_0 = 150$ Hz and $FC_2 = 600$ Hz, respectively. The data were reduced with MANTID [55] and analyzed using DAVE [56] software, while we employed custom software to refine the CEF spectrum of the highly stuffed powder samples.

III. POWDER DIFFRACTION REFINEMENT

We first discuss the results of our refinement for neutron powder diffraction data collected at POWGEN [50] at $T = 300$ K. The Rietveld refinements of the POWGEN data sets were done independently using JANA2006 [51] and FULLPROF [52]. The starting structural model assumed in the refinements was that of the stoichiometric compound, $Yb_2Ti_2O_7$, and this model has been found to yield poor agreement with the data sets. A second model was then used to permit occupancy of Yb ions at the 16*c* Ti site according to the formula $Yb_{2+x}Ti_{2-x}O_{7-y}$, and the best solutions according to this model were found using both JANA2006 and FULLPROF. The resulting solutions for each of the compounds from JANA2006 were put into FULLPROF and vice versa and were further refined. The resulting best-fit parameters were found to be the same within error, confirming the robustness of

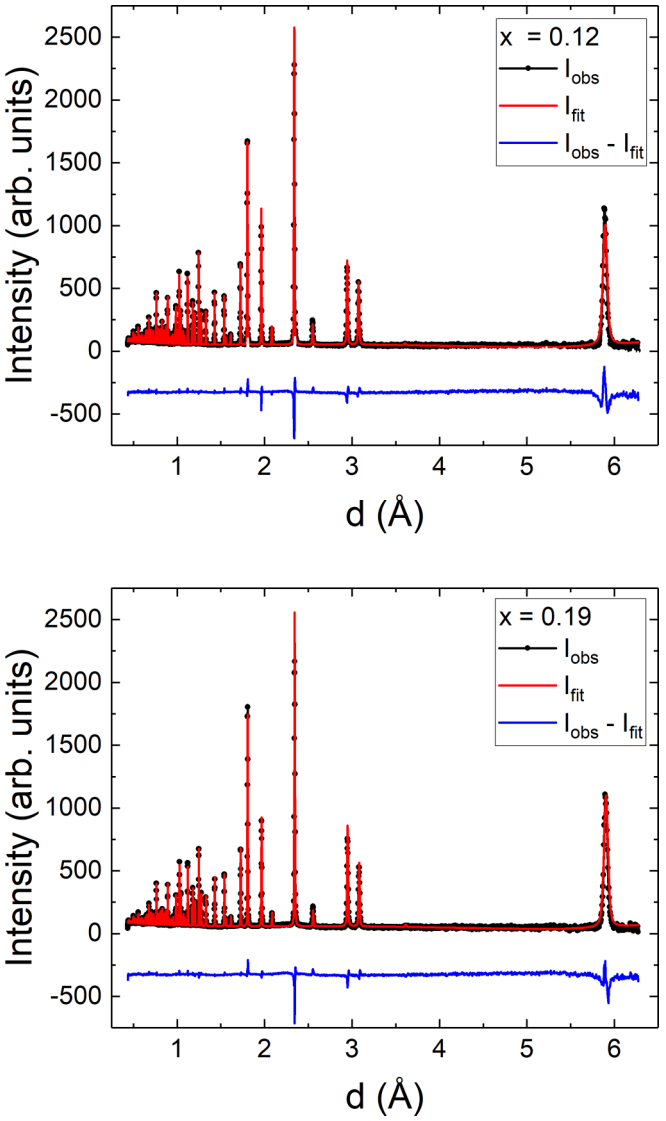

FIG. 2. Rietveld powder neutron diffraction refinements of the $Yb_{2+x}Ti_{2-x}O_{7-y}$ stuffed crystals: The refined chemical formulas for the two compounds are $Yb_{2.122}Ti_{1.878}O_{6.939}$ and $Yb_{2.192}Ti_{1.808}O_{6.904}$, giving $x = 0.12$ and $x = 0.19$, respectively, consistent with the approximate stoichiometry of the starting materials in the crystal growth. As can be seen, the refinement agrees well with the experimental data with $R = 4.6$ and $R = 4.3$ obtained for the two highly stuffed samples, $x = 0.12$ and $x = 0.19$, respectively.

the fits conducted on these samples. The resulting fits for $x = 0.12$ and $x = 0.19$ are shown in Fig. 2 and agree well with the data, with R factors of 4.6 and 4.3, respectively. These R factors compare well with previous refinements done on stuffed ytterbium titanate pyrochlores [27,57]. The high-quality neutron powder diffraction refinements shown in Fig. 2 give unit cell parameters of $a = 10.061(2)$ Å for the $x = 0.12$ sample and of $a = 10.079(3)$ Å for the $x = 0.19$ sample. The fact that the length of the unit cell gets bigger as the stuffing x increases is a direct consequence of the oxygen vacancies; the Coulomb repulsion of the cations left unshielded by the vacancy tends to push all the ions away from each other, increasing the size of the unit cell. Moreover,

TABLE I. Summary of the Rietveld refinement results obtained from neutron powder diffraction experiments conducted at POWGEN on the two highly stuffed samples of $Yb_2(Ti_{2-x}Yb_x)O_{7-y}$ with $x = 0.12$ and $x = 0.19$ at $T = 300$ K.

Atom	x	y	z	Site	Occupancy
		$x = 0.12$ sample			
Yb	0.625	0.125	0.125	16*d*	1
Ti	0.125	0.125	0.125	16*c*	0.939(2)
Yb	0.125	0.125	0.125	16*c*	0.061(2)
O(2)	0.456(8)	0.25	0.25	48*f*	0.992(11)
O(1)	0.5	0.5	0.5	8*b*	0.927(6)
		$x = 0.19$ sample			
Yb	0.625	0.125	0.125	16*d*	1
Ti	0.125	0.125	0.125	16*c*	0.904(2)
Yb	0.125	0.125	0.125	16*c*	0.096(2)
O(2)	0.458(10)	0.25	0.25	48*f*	0.987(12)
O(1)	0.5	0.5	0.5	8*b*	0.910(7)

our refinement showed that these vacancies are mainly located on the O(1) sites of the pyrochlore lattice, confirming the analysis in Ref. [53]. The refined chemical formulas for the two highly stuffed powders are $Yb_{2.122}Ti_{1.878}O_{6.939}$ and $Yb_{2.192}Ti_{1.808}O_{6.904}$, giving a stuffing level of $x = 0.12$ and $x = 0.19$, respectively, in agreement with the approximate stoichiometry of the starting materials used in the crystal growth (see Tables I and II). Note that the stoichiometric ($x = 0$) and lightly stuffed ($x = 0.05$) samples have previously been characterized by powder diffraction techniques by Ross *et al.* [27].

IV. CRYSTAL FIELD ANALYSIS OF INELASTIC NEUTRON SPECTROSCOPY

Inelastic neutron scattering spectra taken at $T = 5$ K on all four powder samples of $Yb_{2+x}Ti_{2-x}O_{7-y}$ studied are shown in Figs. 3 and 4. Figure 3 shows relatively low energy data taken with $E_i = 150$ meV, while Fig. 4 shows relatively high energy data taken with $E_i = 500$ meV. Most of the spectral weight at these high energies is due to CEF excitations from the ground-state doublet appropriate for Yb^{3+} as the lowest CEF excitation is at ∼76 meV and the highest-energy

TABLE II. Results from Rietveld refinement for the degree of stuffing x and the lattice parameter a for the four compounds of $Yb_2(Ti_{2-x}Yb_x)O_{7-y}$ studied. The values for the pure and lightly stuffed compounds, $x = 0.000(1)$ and $x = 0.046(4)$, were refined at $T = 250$ K and were retrieved from Ref. [34]. The values of the lattice parameter obtained for $x = 0.122(4)$ and $x = 0.192(3)$ were those obtained for the $T = 300$ K neutron diffraction data reported in Table I.

Degree of stuffing x	a (Å)
0.000(1)	10.020(3)
0.046(4)	10.029(4)
0.122(4)	10.061(2)
0.192(3)	10.079(3)

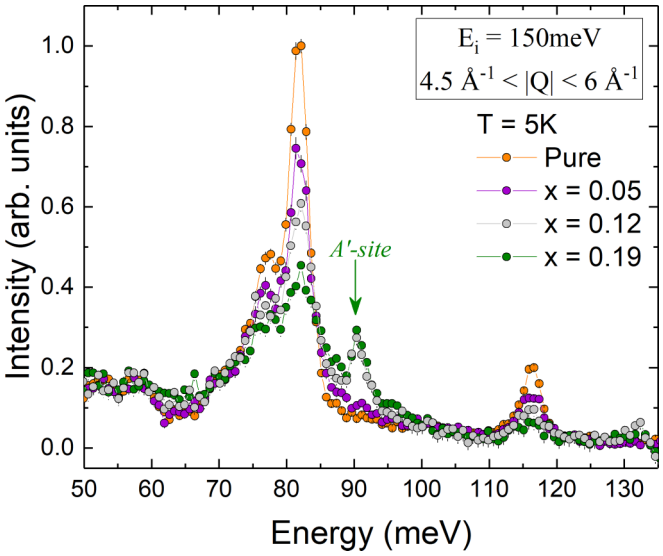

FIG. 3. The measured neutron scattering intensity obtained from $E_i = 150$ meV data sets for four powder samples of $Yb_{2+x}Ti_{2-x}O_{7-y}$ is shown. An empty-can data set has been subtracted from all data. The difference between the CEF intensities of the four samples is evident. In the stoichiometric compound (orange points) there are only three visible levels at ∼76, 81, and 116 meV; their intensities decrease as the system is stuffed (as x increases), and a new CEF level at ∼90 meV appears. The intensities have been scaled in proportion to the actual sample masses.

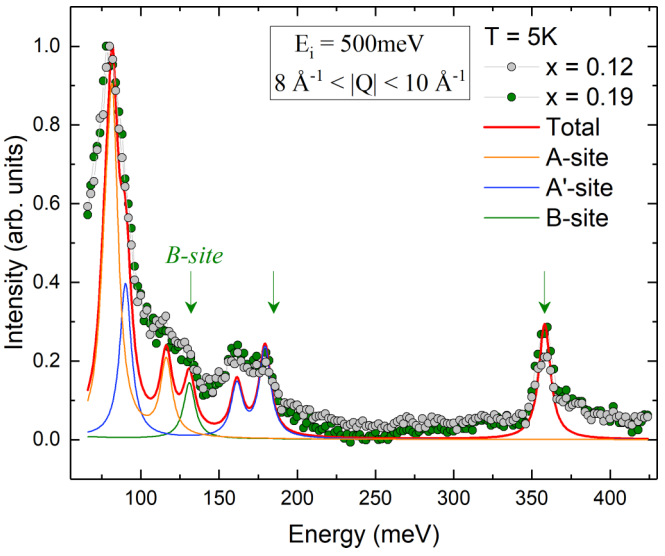

FIG. 4. The measured neutron scattering intensity obtained from $E_i = 500$ meV data sets for two highly stuffed samples of $Yb_{2+x}Ti_{2-x}O_{7-y}$ are shown. An empty-sample-can subtraction has been employed. The calculated spectrum (red line) shows good agreement with the experimental data (gray and green dots for the $x = 0.12$ and $x = 0.19$ samples, respectively). The three different contributions to the total spectrum are highlighted in orange for the stoichiometric A sites, blue for the oxygen-deficient A' sites, and green for stuffed Yb^{3+} ions at the B sites. The total calculated intensity from all three sites is shown in red.

phonons in this pyrochlore family are known to extend to only 100 meV [58]. Inelastic neutron scattering data for the highly stuffed samples ($x = 0.12$ and $x = 0.19$) are shown in Fig. 5 as a function of temperature at both $T = 5$ K [Figs. 5(a) and 5(b)] and $T = 200$ K [Figs. 5(c) and 5(d)].

CEF excitations have several important characteristics: as single-ion properties, the CEFs tend to be dispersionless, and the $|Q|$ dependence of their intensities is largely determined by the magnetic form factor of the magnetic ion involved. They also display temperature dependence that reflects the population distribution of the CEF levels. Given that the lowest-energy CEF excited state is at ∼76 meV for all temperatures below room temperature, we expect no excited states to be thermally populated. These features can be used to distinguish the CEF levels from the background and from other elementary excitations, particularly phonons.

As the temperature is increased, the spectrum becomes broader in energy, in agreement with previous observations by Gaudet *et al.* [45]. This is not a thermal population effect but the result of the CEFs acquiring finite lifetimes due to interactions with other excitations, notably phonons. With the exception of the A site Yb^{3+} CEF excitations, the normalized intensity of the inelastic features in the spectrum is stronger for the $x = 0.19$ sample than for the $x = 0.12$ sample, as expected, reflecting the higher level of stuffing.

Crystal field refinement

In order to analyze the neutron scattering data and fit the CEF excitations, we developed a calculation based on the point-charge model [59] using Stevens's formalism [60]. The former neglects the overlap between the orbitals and any relativistic corrections, while the latter is a mathematical tool to write an expansion of the Coulomb potential of the crystal based on the symmetries of the environment that surrounds

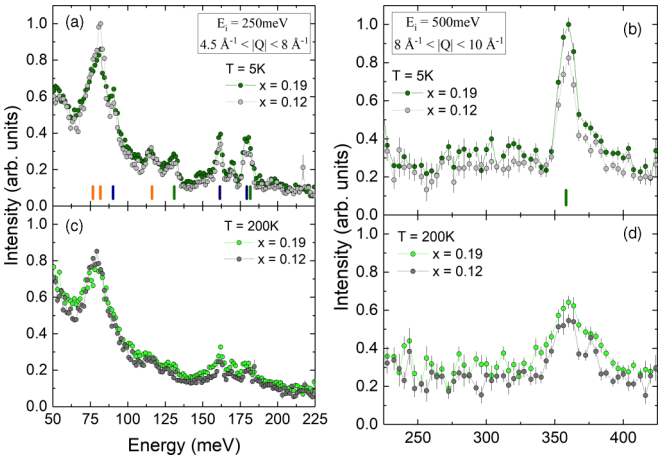

FIG. 5. Comparison of the normalized intensities of the inelastic neutron spectrum at $T = 5$ K (top panels) and $T = 200$ K (bottom panels) for incident energies $E_i = 250$ meV and $E_i = 500$ meV. The inelastic peak at ∼358 meV arises due to Yb^{3+} at B sites. The calculated energy eigenvalues associated with all three of the A, A', and B Yb^{3+} sites are shown as the fiducial lines at the bottom of (a) and (b). The color scheme used for the fiducial lines is the same as in Fig. 4, and we see that the CEF model describes the inelastic spectra below 400 meV very well.

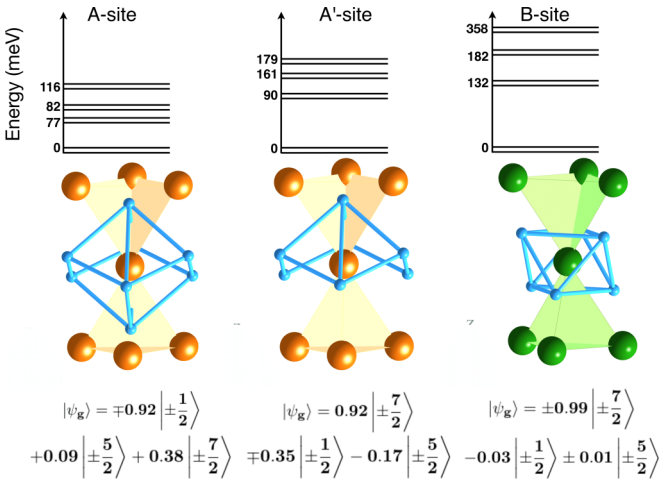

FIG. 6. Left: At the stoichiometric A sites, the ligands are located on the vertex of a scalenohedron, a cube distorted along the diagonal. The blue spheres represent the six O(2) ions and two O(1) ions around the A site Yb^{3+}. The O(1) sites are located along the axis connecting the centers of two tetrahedra. Middle: The A' sites correspond to A sites with one O(1) vacancy that breaks the symmetry of the scalenohedron. Right: At the B sites, the environment is a trigonal antiprism made of six O(2) ions; green spheres represent the position of Ti^{4+} ions or the position of the stuffed Yb^{3+} ions. The top panels show the corresponding energy eigenvalues associated with each environment. Note that the energy scale is approximate and serves only to guide the eye for comparison of the CEF excitation energies. The bottom panels give the three largest contributions to the ground-state energy eigenfunctions associated with each environment.

the magnetic ion. In our samples, the magnetic rare-earth ion is assumed to be sitting in three different environments: stoichiometric A sites, oxygen deficient A' sites, and B sites (see Fig. 6). Notice that we have rotated the reference system in order to align the local $\langle 111\rangle$ direction along $\hat{z}$.

In general the Coulomb potential of the crystal can be expressed using a linear combination of tesseral harmonics as follows:

$$V(x,y,z) = \frac{q_j}{4\pi\epsilon_0}\sum_{n=0}^{\infty}\frac{r^n}{R_j^{(n+1)}}\left\{\sum_m \frac{4\pi}{(2n+1)} \times Z_{nm}(x_j,y_j,z_j)Z_{nm}(x,y,z)\right\}. \quad (1)$$

Here q_j is the charge of the ligand, R_j is the position of the ligand, and $Z_{nm}(x_j,y_j,z_j)$ is the tesseral harmonic [59]. If we center our reference system on the magnetic ion, we can rewrite the previous equation in the following way:

$$V(x,y,z) = \frac{1}{4\pi\epsilon_0}\sum_n^{\infty}\sum_m r^n \gamma_{nm} Z_{nm}(x,y,z), \quad (2)$$

where, for k ligands,

$$\gamma_{nm} = \sum_{j=1}^{k}\frac{q_j}{R_j^{(n+1)}}\frac{4\pi}{2n+1}Z_{nm}(x_j,y_j,z_j). \quad (3)$$

Equation (3) gives the coefficients of the linear combination of the tesseral harmonics. For every point group, only a few terms in the expansion are nonzero (see, e.g., Ref. [61]), and these terms coincide with the number of Stevens operators we use in our Hamiltonian.

The point group of both the scalenohedron at the A site and the trigonal antiprism at the B site is D_{3d}, and thus, following Prather's convention [62], only the terms $Z_{20}, Z_{40}, Z_{43}, Z_{60}, Z_{63}$, and Z_{66} survive in our expansion. This convention states that the highest rotational C_3 axis of the system must be rotated along $\hat{z}$ and one of the C_2 axis must be rotated along $\hat{y}$, ensuring in this way that we have the minimum number of terms in the Coulomb expansion.

Finally, we can use the so-called Stevens operators equivalence method to evaluate the matrix elements of the crystalline potential between coupled wave functions specified by one particular value of the total angular momentum J. This method states that, if $f(x,y,z)$ is a Cartesian function of given degree, then to find the operator equivalent to such a term one replaces x, y, z with J_x, J_y, J_z, respectively, keeping in mind the commutation rules between these operators. This is done by replacing products of x, y, z by the appropriate combinations of J_x, J_y, J_z, divided by the total number of combinations. Note that, although it is conventional to use J or L in the equivalent-operator method, all factors of $\hbar$ are dropped when evaluating the matrix elements.

As we are studying the ground state of a rare-earth system, without an external magnetic field applied, S^2, L^2, J^2, and J_z are good quantum numbers. Thus, the CEF Hamiltonian can now be written as

$$H_{\mathrm{CEF}} = \mathrm{const}\sum_{nm}\left[\frac{e^2}{4\pi\epsilon_0}\gamma_{nm}\langle r^n\rangle\theta_n\right]O_n^m = \sum_{nm}\underbrace{\left[A_n^m\langle r^n\rangle\theta_n\right]}_{B_{nm}}O_n^m = \sum_{nm}B_{nm}O_n^m, \quad (4)$$

where γ_{nm} is the same coefficient as in Eq. (3), e is the electron charge, ϵ_0 is the vacuum permittivity, $\langle r^n\rangle$ is the expectation value of the radial part of the wave function, θ_n is a numerical factor that depends on the rare-earth ion [59], const is a constant to normalize the tesseral harmonics, and O_n^m are the Stevens operators.

The terms $A_n^m\langle r^n\rangle\theta_n$ are commonly called crystal field parameters, and they coincide with the parameters we fit in our calculation. A general form of the Hamiltonian for our system is therefore

$$H_{\mathrm{CEF}} = B_{20}O_2^0 + B_{40}O_4^0 + B_{43}O_4^3 + B_{60}O_6^0 + B_{63}O_6^3 + B_{66}O_6^6. \quad (5)$$

These equations are nonlinear, so we cannot write a closed system to solve the problem and identify a unique solution. We thus decided to use our Hamiltonian as a function of the six CEF parameters and to simultaneously fit these to experimental quantities of interest: the energy of the CEF excitations and the relative intensities of the transitions between the CEF levels. The resulting refined CEF parameters are then used to calculate the inelastic neutron spectrum for a direct comparison with the data set. Table III shows the best CEF parameters which were found minimize χ^2 in the fitting procedure along with

TABLE III. Refinement of the CEF parameters and energy eigenvalues at each of the three Yb^{3+} sites from fits to the inelastic spectra data set at the three sites and relative energy levels. All energy eigenvalues are doublets (d), as required by Kramers's theorem.

A Site	*A′* Site	*B* Site
Crystal field parameters (meV)		
$B_2^0 = 1.1$	$B_2^0 = -3.9860$	$B_2^0 = -4.8744$
$B_4^0 = -0.0591$	$B_4^0 = -0.002186$	$B_4^0 = -0.1407$
$B_4^3 = 0.3258$	$B_4^3 = 1.0655$	$B_4^3 = 1.47542$
$B_6^0 = 0.00109$	$B_6^0 = 0.001533$	$B_6^0 = -0.004862$
$B_6^3 = 0.0407$	$B_6^3 = 0.049192$	$B_6^3 = -0.1117$
$B_6^6 = 0.00727$	$B_6^6 = 0.01666$	$B_6^6 = 0$
Calculated spectrum (meV)		
0.0(*d*)	0.0(*d*)	0.0(*d*)
76.72(*d*)	90.17(*d*)	130.98(*d*)
81.76(*d*)	161.38(*d*)	181.79(*d*)
116.15(*d*)	179.36(*d*)	358.14(*d*)

the energy eigenvalues corresponding to the CEF excitations of Yb^{3+} ions out of the ground state at the *A*, *A′*, and *B* sites.

V. RESULTS AND DISCUSSION

The CEFs originate primarily from the "cage" of O^{2-} ions surrounding the cations, lifting the $(2J+1)$-fold degeneracy of the $J = 7/2$ ground-state manifold appropriate for Yb^{3+}. The case for Yb^{3+} is relatively straightforward as its odd number (13) of $4f$ electrons means that it satisfies Kramers's theorem, and all the CEF states are at least doubly degenerate, so with $J = 7/2$ there can be at most three CEF transitions from the ground state.

We considered the three local Yb^{3+} environments shown in Fig. 6. These are Yb^{3+} in an *A*-site environment with a full complement of eight neighboring O^{2-} ions, Yb^{3+} in an *A*-site environment with one O^{2-} vacancy (referred to as an *A′* site), and a Yb^{3+} ion in a *B*-site environment with a full complement of six neighboring O^{2-} ions. The *A* site O^{2-} environment consists of a cube distorted along the local [111] directions. Six O(2) ions are located on a plane perpendicular to this direction and a threefold rotation axis. Two additional O(1) ions are located along the local [111] axis. In other titanate pyrochlores, the O(1) sites are known to have a higher probability of hosting vacancies than the O(2) sites [53], a result which we confirmed here for $Yb_{2+x}Ti_{2-x}O_{7-y}$ using powder neutron diffraction. By contrast, the environment at the *B* site is a trigonal antiprism made of six O(2) oxygen ions. Additional local Yb^{3+} environments, such as an *A* site Yb^{3+} with an O(2) vacancy or with two vacancies, were assumed to be unlikely at the stuffing levels considered here.

The unpolarized neutron partial differential magnetic cross section can be written within the dipole approximation as [63]

$$\frac{d^2\sigma}{d\Omega dE'} = C\frac{k_f}{k_i}F(|Q|)S(|Q|,\omega), \quad (6)$$

where Ω is the scattered solid angle, $\frac{k_f}{k_i}$ is the ratio of the scattered and incident momentum of the neutron, C is a constant, and $F(|Q|)$ is the magnetic form factor of the magnetic

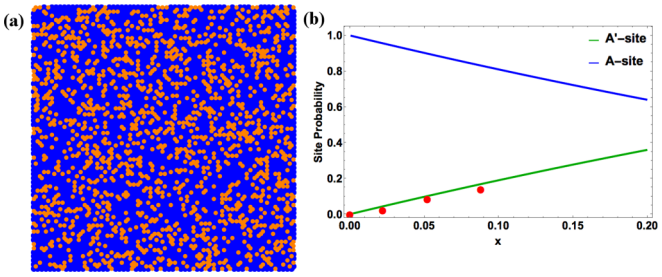

FIG. 7. Preponderance of *A* and *A′* sites within the pyrochlore lattice as a function of stuffing: (a) Projection of the $64 \times 64 \times 64$ supercell used in the Monte Carlo simulation. The orange dots represent oxygen ions removed from the calculation. (b) Histogram showing the distribution of *A* (blue line) and *A′* sites (green line) in the lattice as a function of the stuffing. The red points represents the experimental intensities of the 90 meV CEF level extrapolated using the pure compound as background. This agreement confirms that this 90 meV CEF transition originates from an *A′* site.

Yb^{3+} ion. The scattering function $S(|Q|,\hbar\omega)$ gives the relative scattered intensity due to transitions between different CEF levels. At constant temperature and wave vector $|Q|$, we have

$$S(|Q|,\hbar\omega) = \sum_{i,i'} \frac{\left(\sum_\alpha |\langle i|J_\alpha|i'\rangle|^2\right)e^{-\beta E_i}}{\sum_j e^{-\beta E_j}} F(\Delta E + \hbar\omega), \quad (7)$$

where $\alpha = x,y,z$ and $F(\Delta E + \hbar\omega) = F(E_i - E_{i'} + \hbar\omega)$ is a Lorentzian function which ensures energy conservation as the neutron induces transitions between the CEF levels $i \rightarrow i'$ that possess a finite-energy width or inverse lifetime.

Figure 3 shows a comparison of the data from the four powder $Yb_{2+x}Ti_{2-x}O_{7-y}$ samples at relatively low energies, using incident neutrons with $E_i = 150$ meV. The intensity scale has been normalized to sample mass. The stoichiometric, $x = 0$, and lightly stuffed, $x = 0.05$, samples show only the three *A* site CEF transitions at ~76, 81, and 116 meV, as previously reported [45]. We clearly observe the growth of a new CEF at ~91 meV, which we will attribute to *A′*-site Yb^{3+}, as a function of increasing stuffing x. This is quantitatively borne out by a Monte Carlo simulation which shows that its normalized intensity scales in proportion to x. Assuming that oxygen atoms are removed at random, we performed a simple Monte Carlo simulation to calculate the relative preponderance of *A* to *A′* sites in the lattice as a function of the stuffing level x. Assuming that each *A* and *A′* site contributes independently to the intensity of the spectrum, we can argue that the intensity of the transition at 91 meV should be proportional to this ratio.

For this calculation we created a supercell consisting of $64 \times 64 \times 64$ unit cells filled with random vacancies located only at the O(1) position. Due to the symmetry of the pyrochlore lattice each Yb^{3+} ion at an *A* site has only two O(1) ions as the first-nearest neighbor; thus, we calculated how many ions have no vacancies and how many have a single vacancy. The calculation was repeated for 10 000 realizations of disorder. Figure 7 shows the results of this analysis, with the conclusion that the transition at 91 meV originates from *A′* sites, and its intensity is directly proportional to the number of vacancies in the system.

The CEF spectrum at energies above 100 meV is shown in Fig. 4 for the highly stuffed ($x = 0.12$ and 0.19) samples, as measured with $E_i = 500$ meV neutrons. One observes clear excitations above the 116 meV CEF excitation associated with the stoichiometric A site's most energetic CEF level. Of particular note is the well-isolated CEF excitation at 358 meV which we associate with Yb^{3+} at the B site, whose intensity scales between the two highly stuffed samples, $x = 0.12$ and 0.19, in proportion to x. The stoichiometric ($x = 0$) and lightly stuffed ($x = 0.05$) samples were measured at high energies with $E_i = 700$ meV neutrons, and the 358 meV CEF excitation is not visible for either.

The energies and relative intensities of all the CEF excitations measured below ~400 meV were fit as described above, assuming the CEF parameters previously established for the stoichiometric sample ($x = 0$) [45]. The new CEF parameters and energies for the A' site and B site are tabulated along with those for the A site Yb^{3+} in Table III. The results for both the CEF intensities and the CEF energy eigenvalues are shown as the solid lines in Fig. 4 for the highly stuffed ($x = 0.12$ and $x = 0.19$) samples at base temperature, $T = 5$ K. Figure 5 shows higher-energy-resolution, inelastic neutron scattering below 225 meV energy transfer, obtained with $E_i = 250$ meV, as well as the same $E_i = 500$ meV data for the highly stuffed samples ($x = 0.12$ and $x = 0.19$) at $T = 5$ K [Figs 5(a) and 5(b)] and at $T = 200$ K [Figs. 5(c) and 5(d)]. For reference, the energies associated with the nine CEF transitions from the A, A', and B sites, as calculated in our fit, are shown as fiducial lines in Figs. 5(a) and 5(b). One can see that virtually all inelastic features in the range from 75 to 400 meV can be identified using this model, and these excitations decrease in intensity and broaden somewhat in energy on warming to $T = 200$ K, shown in Figs. 5(c) and 5(d), as expected for CEF excitations. The description of all CEF levels below ~400 meV is therefore very good, and the resulting CEF energy eigenvalues are shown for the A-, A'-, and B-site Yb^{3+} in the top panel of Fig. 6. The bandwidth of the CEF excitations is much larger for Yb^{3+} in the defective environments, with the defective B site environment giving the largest bandwidth, consistent with this Yb^{3+} ion experiencing the largest electric fields and their gradients.

The determination of the CEF parameters allows a determination of the g-tensor characterizing the anisotropy, as well as the moment size associated with the ground-state doublet of Yb^{3+} at the A, A', and B sites. The resulting eigenfunctions within the Yb^{3+} ground-state doublets are shown in the bottom panel of Fig. 6. The corresponding anisotropic g-tensor values are $g_\perp = 3.69 \pm 0.15$, $g_z = 1.92 \pm 0.20$ for Yb^{3+} at the A site; $g_\perp = 1.5 \pm 0.2$, $g_z = 6.8 \pm 0.7$ for Yb^{3+} at the A' site; and $g\perp = 0.07 \pm 0.03$, $g_z = 8.0 \pm 0.8$ for Yb^{3+} at the B site. The A-site Yb^{3+} moment was previously known to display XY anisotropy [45]. These results show both the A'-site and B-site Yb^{3+} moments to possess Ising-like anisotropies, with the B-site Yb^{3+} Ising anisotropy being stronger than that associated with the A' site. Such a change in anisotropy between the A site and the defective B and A' Yb^{3+} sites was predicted on the basis of point-charge calculations [45] but has now been directly verified with these measurements. The ground-state moments associated with the A, A', and B sites are found to be $\mu = 2.07\mu_B$, $\mu = 3.5\mu_B$, and $\mu = 4.0\mu_B$, respectively [45]. While dipolar interactions are expected to be relatively weak in

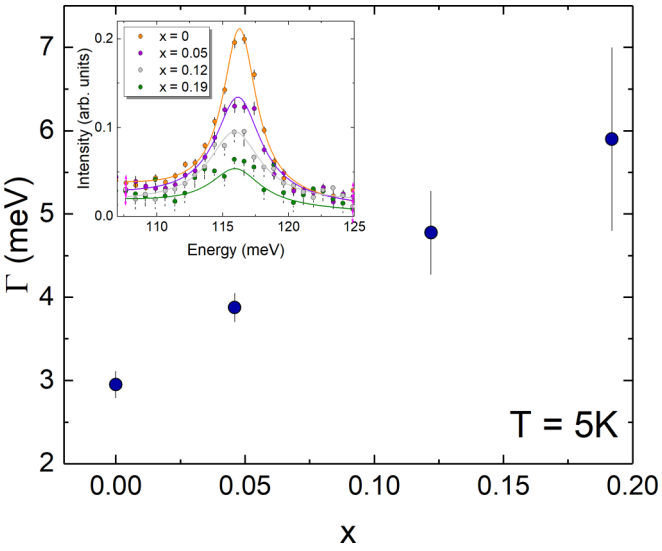

FIG. 8. The systematic broadening of the CEF intrinsic energy width which is observed with increased stuffing x in $Yb_{2+x}Ti_{2-x}O_{7-y}$, as obtained from the Lorentzian line-shape analysis discussed in the text. The inset shows the inelastic neutron scattering near the ~116 meV CEF transition and the resulting fits performed with a Lorentzian line shape.

$Yb_2Ti_2O_7$ due to the low moment size, they scale as the square of the moment, and thus, larger defective moments would tend to produce a strong, random perturbation on the dipole sum.

It is also clear that the A-site CEF transitions develop significant energy broadening with increasing stuffing. This can be broadly appreciated in Fig. 3 and is examined quantitatively in Fig. 8, where attention is focused on the ~116 meV A-site Yb^{3+} CEF transition, which is well separated in energy from any other transition for all powder samples. The energy width of the CEF excitations can be examined by fitting the data, shown in the inset of Fig. 8, utilizing a damped harmonic oscillator (DHO) line shape for the 116 meV CEF transitions. At the energy transfers and temperatures of interest, the DHO can be approximated by a single Lorentzian, the form of which is given by

$$L(E) = \frac{1}{\pi} \frac{\frac{\Gamma_{obs}}{2}}{(E - \Delta E)^2 + (\frac{\Gamma_{obs}}{2})^2}. \quad (8)$$

This is a Lorentzian function of energy with width Γ_{obs} centered on the energy of the CEF transition. This form convolutes both the intrinsic energy width and that arising from the instrumental resolution, which are assumed to add in quadrature. The intrinsic energy width or inverse lifetime of the 116 meV CEF excitation for each of the four powder samples was extracted from this analysis and is plotted as a function of stuffing x in Fig. 8.

Figure 8 clearly shows the CEF excitations at low temperatures in the crushed single-crystal samples display much larger energy widths than that of the stoichiometric sample. The trend for low-temperature CEF inverse lifetimes to systematically increase with stuffing, previously reported for the stoichiometric ($x = 0$) and lightly stuffed ($x = 0.05$) samples [45], is seen to extend to the largest stuffing level studied, $x = 0.19$.

VI. CONCLUSION

In conclusion, time-of-flight neutron spectroscopy allows the possibility of detecting and distinguishing CEF excitations in complex real materials with relatively low levels of defective environments, and we have demonstrated this for the quantum spin ice candidate pyrochlore magnet $Yb_{2+x}Ti_{2-x}O_{7-y}$. Such detailed information is particularly important for the case of $Yb_2Ti_2O_7$, as its ground state displays unusually strong sensitivity to stoichiometry. Our results specifically show Yb^{3+} moments in stuffed and oxygen-deficient environments display Ising anisotropy, rather than the XY local anisotropy displayed by the stoichiometric moments. Such defective Yb^{3+} moments are also considerably larger than their stoichiometric counterparts, and these, at a minimum, would tend to randomize dipolar interactions. Both of these manifestations of stuffing can be important for ground-state selection in real samples of $Yb_{2+x}Ti_{2-x}O_{7-y}$ and may underlie the ground state's extreme sensitivity to stoichiometry in this family of quantum magnets.

Note added. Recently, we became aware of two papers that discuss the role of stuffing in iridate pyrochlores [64], and atomic and electronic structure in stuffed $Yb_2Ti_2O_7$ [65].

ACKNOWLEDGMENTS

Research conducted at McMaster University was supported by the Natural Sciences and Engineering Research Council of Canada (NSERC). We acknowledge useful discussions with A. Aczel, C. Balz, L. Balents, G. Ehlers, M. D. Lumsden, S. E. Nagler, and K. A. Ross. We are very grateful for the instrument and sample environment support provided during our inelastic neutron scattering measurements. The experiments which were performed at the Spallation Neutron Source at Oak Ridge National Laboratory were sponsored by the US Department of Energy, Office of the Basic Energy Sciences, Scientific User Facilities Division.

[1] C. Lacroix, P. Mendels, and F. Mila, *Introduction to Frustrated Magnetism* (Springer, Berlin, 2011).
[2] J. S. Gardner, M. J. P. Gingras, and J. E. Greedan, Rev. Mod. Phys. **82**, 53 (2010).
[3] M. J. Harris, S. T. Bramwell, D. F. McMorrow, T. Zeiske, and K. W. Godfrey, Phys. Rev. Lett. **79**, 2554 (1997).
[4] A. P. Ramirez, A. Hayashi, R. J. Cava, R. Siddharthan, and B. S. Shastry, Nature (London) **399**, 333 (1999).
[5] B. C. den Hertog and M. J. P. Gingras, Phys. Rev. Lett. **84**, 3430 (2000).
[6] S. T. Bramwell and M. J. P. Gingras, Science **294**, 1495 (2001).
[7] C. Castelnovo, R. Moessner, and S. L. Sondhi, Nature (London) **451**, 42 (2008).
[8] L. Clark, G. J. Nilsen, E. Kermarrec, G. Ehlers, K. S. Knight, A. Harrison, J. P. Attfield, and B. D. Gaulin, Phys. Rev. Lett. **113**, 117201 (2014).
[9] S. Petit, E. Lhotel, B. Canals, M. Ciomaga Hatnean, J. Ollivier, H. Mutka, E. Ressouche, A. R. Wildes, M. R. Lees, and G. Balakrishnan, Nat. Phys. **12**, 746 (2016).
[10] K. A. Ross, L. Savary, B. D. Gaulin, and L. Balents, Phys. Rev. X **1**, 021002 (2011).
[11] N. R. Hayre, K. A. Ross, R. Applegate, T. Lin, R. R. P. Singh, B. D. Gaulin, and M. J. P. Gingras, Phys. Rev. B **87**, 184423 (2013).
[12] J. D. Thompson, P. A. McClarty, H. M. Rønnow, L. P. Regnault, A. Sorge, and M. J. P. Gingras, Phys. Rev. Lett. **106**, 187202 (2011).
[13] R. Applegate, N. R. Hayre, R. R. P. Singh, T. Lin, A. G. R. Day, and M. J. P. Gingras, Phys. Rev. Lett. **109**, 097205 (2012).
[14] O. Benton, O. Sikora, and N. Shannon, Phys. Rev. B **86**, 075154 (2012).
[15] L. Savary and L. Balents, Phys. Rev. Lett. **108**, 037202 (2012).
[16] R. M. D'Ortenzio, H. A. Dabkowska, S. R. Dunsiger, B. D. Gaulin, M. J. P. Gingras, T. Goko, J. B. Kycia, L. Liu, T. Medina, T. J. Munsie, D. Pomaranski, K. A. Ross, Y. J. Uemura, T. J. Williams, and G. M. Luke, Phys. Rev. B **88**, 134428 (2013).
[17] J. D. Thompson, P. A. McClarty, and M. J. P. Gingras, J. Phys.: Condens. Matter **23**, 164219 (2011).
[18] L. Savary and L. Balents, Phys. Rev. B **87**, 205130 (2013).
[19] K. Kimura, S. Nakatsuji, J.-J. Wen, C. Broholm, M. B. Stone, E. Nishibori, and H. Sawa, Nat. Commun. **4**, 1934 (2013).
[20] M. J. P. Gingras and P. A. McClarty, Rep. Prog. Phys. **77**, 056501 (2014).
[21] L. D. Pan, S. W. Kim, A. Ghosh, C. M. Morris, K. A. Ross, E. Kermarrec, B. D. Gaulin, S. M. Koohpayeh, O. Tchernyshyov, and N. P. Armitage, Nat. Commun. **5**, 4970 (2014).
[22] L. D. Pan, N. J. Laurita, K. A. Ross, B. D. Gaulin, and N. P. Armitage, Nat. Phys. **12**, 361 (2016).
[23] N. Hamachi, Y. Yasui, K. Araki, S. Kittaka, and T. Sakakibara, AIP Adv. **6**, 055707 (2016).
[24] H. Blöte, R. Wielinga, and W. Huiskamp, Physica **43**, 549 (1969).
[25] P. Dalmas de Réotier, V. Glazkov, C. Marina, A. Yaouanc, P. C. M. Gubbens, S. Sakarya, P. Bonville, A. Amato, C. Baines, and P. J. C. King, Phys. B (Amsterdam, Neth.) **374-375**, 145 (2006).
[26] A. Yaouanc, P. Dalmas de Réotier, C. Marin, and V. Glazkov, Phys. Rev. B **84**, 172408 (2011).
[27] K. A. Ross, Th. Proffen, H. A. Dabkowska, J. A. Quilliam, L. R. Yaraskavitch, J. B. Kycia, and B. D. Gaulin, Phys. Rev. B **86**, 174424 (2012).
[28] A. M. Hallas, J. Gaudet, and B. D. Gaulin, Annu. Rev. Condens. Matter Phys. **9**, 105 (2018).
[29] Y. Yasui, M. Soda, S. Iikubo, M. Ito, M. Sato, N. Hamaguchi, T. Matsushita, N. Wada, T. Takeuchi, N. Aso, and K. Kakurai, J. Phys. Soc. Jpn. **72**, 3014 (2003).
[30] L.-J. Chang, S. Onoda, Y. Su, Y. J. Kao, K. D. Tsuei, Y. Yasui, K. Kakurai, and M. R. Lees, Nat. Commun. **3**, 992 (2012).
[31] J. Gaudet, K. A. Ross, E. Kermarrec, N. P. Butch, G. Ehlers, H. A. Dabkowska, and B. D. Gaulin, Phys. Rev. B **93**, 064406 (2016).
[32] A. Scheie, J. Kindervater, S. Säubert, C. Duvinage, C. Pfleiderer, H. J. Changlani, S. Zhang, L. Harriger, K. Arpino, S. M. Koohpayeh, O. Tchernyshyov, and C. Broholm, Phys. Rev. Lett. **119**, 127201 (2017).
[33] K. A. Ross, J. P. C. Ruff, C. P. Adams, J. S. Gardner, H. A. Dabkowska, Y. Qiu, J. R. D. Copley, and B. D. Gaulin, Phys. Rev. Lett. **103**, 227202 (2009).

[34] K. A. Ross, L. R. Yaraskavitch, M. Laver, J. S. Gardner, J. A. Quilliam, S. Meng, J. B. Kycia, D. K. Singh, Th. Proffen, H. A. Dabkowska, and B. D. Gaulin, Phys. Rev. B **84**, 174442 (2011).

[35] J. A. Hodges, P. Bonville, A. Forget, A. Yaouanc, P. Dalmas de Réotier, G. André, M. Rams, K. Królas, C. Ritter, P. C. M. Gubbens, C. T. Kaiser, P. J. C. King, and C. Baines, Phys. Rev. Lett. **88**, 077204 (2002).

[36] A. Yaouanc, P. Dalmas de Réotier, P. Bonville, J. A. Hodges, P. C. M. Gubbens, C. T. Kaiser, and S. Sakarya, Phys. B (Amsterdam, Neth.) **326**, 456 (2003).

[37] J. S. Gardner, G. Ehlers, N. Rosov, R. W. Erwin, and C. Petrovic, Phys. Rev. B **70**, 180404 (2004).

[38] S. Bhattacharjee, S. Erfanifam, E. L. Green, M. Naumann, Z. Wang, S. Granovsky, M. Doerr, J. Wosnitza, A. A. Zvyagin, R. Moessner, A. Maljuk, S. Wurmehl, B. Büchner, and S. Zherlitsyn, Phys. Rev. B **93**, 144412 (2016).

[39] P. Bonville, J. A. Hodges, E. Bertin, J. P. Bouchaud, P. Dalmas de Réotier, L. P. Regnault, H. M. Rønnow, J. P. Sanchez, S. Sosin, and A. Yaouanc, Hyperfine Interact. **156**, 103 (2004).

[40] K. E. Arpino, B. A. Trump, A. O. Scheie, T. M. McQueen, and S. M. Koohpayeh, Phys. Rev. B **95**, 094407 (2017).

[41] A. Mostaed, G. Balakrishnan, M. R. Lees, Y. Yasui, L.-J. Chang, and R. Beanland, Phys. Rev. B **95**, 094431 (2017).

[42] J. D. Thompson, P. A. McClarty, D. Prabhakaran, I. Cabrera, T. Guidi, and R. Coldea, Phys. Rev. Lett. **119**, 057203 (2017).

[43] E. Lhotel, S. R. Giblin, M. R. Lees, G. Balakrishnan, L. J. Chang, and Y. Yasui, Phys. Rev. B **89**, 224419 (2014).

[44] E. Kermarrec, J. Gaudet, K. Fritsch, R. Khasanov, Z. Guguchia, C. Ritter, K. A. Ross, H. A. Dabkowska, and B. D. Gaulin, Nat. Commun. **8**, 14810 (2017).

[45] J. Gaudet, D. D. Maharaj, G. Sala, E. Kermarrec, K. A. Ross, H. A. Dabkowska, A. I. Kolesnikov, G. E. Granroth, and B. D. Gaulin, Phys. Rev. B **92**, 134420 (2015).

[46] S. Rosenkranz, A. P. Ramirez, A. Hayashi, R. J. Cava, R. Siddharthan, and B. S. Shastry, J. Appl. Phys. **87**, 5914 (2000).

[47] A. Bertin, Y. Chapuis, P. Dalmas de Réotier, and A. Yaouanc, J. Phys.: Condens. Matter **24**, 256003 (2012).

[48] J. Gaudet, A. M. Hallas, A. I. Kolesnikov, and B. D. Gaulin, Phys. Rev. B **97**, 024415 (2018).

[49] H. A. Dabkowska and A. B. Dabkowski, in *Springer Handbook of Crystal Growth*, edited by G. Dhanaraj, K. Byrappa, V. Prasad, and M. Dudley (Springer, Berlin, 2010), p. 367.

[50] A. Huq, J. P. Hodges, O. Gourdon, and L. Heroux, Z. Kristallogr. Proc. **1**, 127 (2011).

[51] V. Petricek, M. Dusek, and L. Palatinus, Z. Kristallogr. **229**, 345 (2014).

[52] J. Rodriguez-Carvajal, Phys. B (Amsterdam, Neth.) **192**, 55 (1993).

[53] G. Sala, M. J. Gutmann, D. Prabhakaran, D. Pomaranski, C. Mitchelitis, J. B. Kycia, D. G. Porter, C. Castelnovo, and J. P. Goff, Nat. Mater. **13**, 488 (2014).

[54] G. E. Granroth, A. I. Kolesnikov, T. E. Sherline, J. P. Clancy, K. A. Ross, J. P. Ruff, B. D. Gaulin, and S. E. Nagler, J. Phys. Conf. Ser. **251**, 12058 (2010).

[55] O. Arnold, J. C. Bilheux, J. M. Borreguero, A. Buts, S. I. Campbell, L. Chapon, M. Doucet, N. Draper, R. Ferraz Leal, M. A. Gigg, V. E. Lynch, A. Markvardsen, D. J. Mikkelson, R. L. Mikkelson, R. Miller, K. Palmen, P. Parker, G. Passos, T. G. Perring, P. F. Peterson, S. Ren, M. A. Reuter, A. T. Savici, J. W. Taylor, R. J. Taylor, R. Tolchenov, W. Zhou, and J. Zikovsky, Nucl. Instrum. Methods Phys. Res., Sect. A **764**, 156 (2014).

[56] R. T. Azuah, L. R. Kneller, Y. Qiu, P. L. W. Tregenna-Piggott, C. M. Brown, and J. R. D. Copley, and R. M. Dimeo, J. Res. Natl. Inst. Stand. Technol. **114**, 341 (2009).

[57] V. Peçanha-Antonio, E. Feng, Y. Su, V. Pomjakushin, F. Demmel, L.-J. Chang, R. J. Aldus, Y. Xiao, M. R. Lees, and T. Brückel, Phys. Rev. B **96**, 214415 (2017).

[58] M. Ruminy, M. N. Valdez, B. Wehinger, A. Bosak, D. T. Adroja, U. Stuhr, K. Iida, K. Kamazawa, E. Pomjakushina, D. Prabakharan, M. K. Haas, L. Bovo, D. Sheptyakov, A. Cervellino, R. J. Cava, M. Kenzelmann, N. A. Spaldin, and T. Fennell, Phys. Rev. B **93**, 214308 (2016).

[59] M. T. Hutchings, in *Solid State Physics*, edited by F. Seitz and D. Turnbull, Advances in Research and Applications Vol. 16 (Academic, New York, 1964), pp. 227–273.

[60] K. W. H. Stevens, Proc. Phys. Soc. A **65**, 209 (1952).

[61] U. Walter, J. Phys. Chem. Solids **45**, 401 (1984).

[62] J. L. Prather, *Atomic Energy Levels in Crystals*, NBS Monograph 19 (National Bureau of Standards, Washington, DC, 1961).

[63] G. L. Squires, *Introduction to the Theory of Thermal Neutron Scattering* (Cambridge University Press, Cambridge, 1978).

[64] P. Telang, K. Mishra, A. K. Sood, and S. Singh, Phys. Rev. B **97**, 235118 (2018).

[65] S. S. Ghosh and E. Manousakis, Phys. Rev. B **97**, 245117 (2018).